The Mars crustal magnetic field control of plasma boundary locations and atmospheric loss: MHD prediction and comparison with MAVEN

Xiaohua Fang[1], Yingjuan Ma[2], Kei Masunaga[3], Yaxue Dong[1], David Brain[1], Jasper Halekas[4], Robert Lillis[5], Bruce Jakosky[1], Jack Connerney[6], Joseph Grebowsky[6], and Chuanfei Dong[7]

Xiaohua Fang, Xiaohua.Fang@lasp.colorado.edu

[1]Laboratory for Atmospheric and Space Physics, University of Colorado, Boulder, Colorado, USA

[2]Department of Earth, Planetary and Space Sciences, University of California, Los Angeles, California, USA.

[3]Department of Earth and Planetary Science, University of Tokyo, Tokyo, Japan,

[4]Department of Physics and Astronomy, University of Iowa, Iowa City, Iowa, USA.

This article has been accepted for publication and undergone full peer review but has not been through the copyediting, typesetting, pagination and proofreading process, which may lead to differences between this version and the Version of Record. Please cite this article as doi: 10.1002/2016JA023509

Abstract. We present results from a global Mars time-dependent MHD simulation under constant solar wind and solar radiation impact considering inherent magnetic field variations due to continuous planetary rotation. We calculate the 3-D shapes and locations of the bow shock (BS) and the induced magnetospheric boundary (IMB) and then examine their dynamic changes with time. We develop a physics-based, empirical algorithm to effectively summarize the multi-dimensional crustal field distribution. It is found that by organizing the model results using this new approach, the Mars crustal field shows a clear, significant influence on both the IMB and the BS. Specifically, quantitative relationships have been established between the field distribution and the mean boundary distances and the cross section areas in the terminator plane for both of the boundaries. The model-predicted relationships are further verified by the observations from the NASA Mars At-

[5]Space Sciences Laboratory, University of California, Berkeley, California, USA.

[6]NASA Goddard Space Flight Center, Greenbelt, Maryland, USA.

[7]Department of Astrophysical Sciences and Princeton Plasma Physics Laboratory, Princeton University, Princeton, New Jersey, USA.

mosphere and Volatile EvolutioN (MAVEN) mission. Our analysis shows that the boundaries are collectively affected by the global crustal field distribution, which, however, cannot be simply parameterized by a local parameter like the widely used subsolar longitude. Our calculations show that the variability of the intrinsic crustal field distribution in MSO itself may account for ∼60% of the variation in total atmospheric loss, when external drivers are static. It is found that the crustal field has not only a shielding effect for atmospheric loss, but also an escape-fostering effect by positively affecting the transterminator ion flow cross section area.

Keypoints:

- The Mars crustal field has a clear, significant influence on both the IMB and the BS.
- The global crustal field distribution collectively affects IMB and BS locations.
- The crustal field has both shielding and escape-fostering effects for atmospheric loss.

1. Introduction

With respect to the study of solar wind-planet interactions, Mars is a particularly unique subject, which has no intrinsic dipole magnetic field to shield against the impinging solar wind but has highly nonuniformly distributed crustal magnetic anomalies [*Acuna et al.*, 1998]. The relatively intense crustal magnetic field in the Martian Southern Hemisphere has been reported to have disturbing effects on the ionosphere [e.g., *Krymskii et al.*, 2004; *Gurnett et al.*, 2005; *Withers*, 2009; *Andrews et al.*, 2015; *Dubinin et al.*, 2016] and on plasma boundary locations [e.g., *Crider et al.*, 2002; *Brain et al.*, 2005; *Edberg et al.*, 2008; *Fang et al.*, 2015]. The potential importance of the crustal field on large-scale atmospheric erosion has also been recognized particularly recently [*Ma et al.*, 2004; *Fang et al.*, 2010a, b; *Brain et al.*, 2010; *Nilsson et al.*, 2011; *Ma et al.*, 2014b; *Brecht and Ledvina*, 2014; *Hara et al.*, 2014; *Dong et al.*, 2015; *Fang et al.*, 2015].

The bow shock (BS) and the induced magnetospheric boundary (IMB) or magnetic pileup boundary (MPB) reflect separation and interchange between the solar wind and planetary plasma. Despite numerous studies in the field, it is still poorly understood how (and even whether) the crustal field controls the location and shape of the boundaries. For the MPB/IMB, which are commonly interchangeably used as the lower boundary of the magnetosheath, there is a general consensus that the boundary tends to be displaced at higher altitudes over the stronger crustal field regions [*Crider et al.*, 2002; *Ma et al.*, 2004; *Brain et al.*, 2005; *Dubinin et al.*, 2008; *Edberg et al.*, 2008, 2009; *Fang et al.*, 2015]. This provides strong evidence that the MPB/IMB is significantly affected by the crustal

field. By contrast, the influence of the crustal field on the BS location remains much less well established. There are seemingly contradictory findings in the literature.

For instance, *Mazelle et al.* [2004] and *Edberg et al.* [2008] found that the Mars Global Surveyor (MGS) crossings of the BS were consistently located farther away from the surface in the Southern Hemisphere than in the Northern Hemisphere. This is often explained by the fact that the crustal field strength is significantly higher in the south, implying the crustal field control of the BS. However, these studies at the same time found no apparent dependence of the boundary height either on the subsolar longitude or on the longitude of the observational sites. The insignificant subsolar longitude dependence has also been reported by *Slavin et al.* [1991], *Vignes et al.* [2002], and *Halekas et al.* [2017]. Using Mars Express measurements, *Edberg et al.* [2009] investigated the dependence of the boundaries on the local crustal field strength. By examining the relationship between the extrapolated MPB and BS terminator distances and the locally averaged crustal magnetic pressure around sub-spacecraft points at 400 km altitudes, they obtained a strong correlation for the MPB but again a very weak correlation for the BS. An important question is naturally raised as to whether the crustal field is able to extend its control beyond the MPB/IMB to efficiently impact the BS, which is located at higher altitudes and seems more directly exposed to the solar wind than to the crustal field at the Mars surface. The puzzle is, if the crustal field does control the BS, then why is there a lack of longitudinal or subsolar longitudinal dependence given the significantly inhomogeneous crustal field distribution? If it does not, then what processes sustain the north-south asymmetry of the BS location?

We examine the limitations of the old methodologies. First, the global crustal field distribution, which collectively affects the solar wind-Mars interaction and the boundaries (at least for the MPB/IMB), can not be simplistically represented by a single point position, no matter whether it is the subsolar point, the sub-spacecraft point, or the strongest crustal field location. It is obvious that these single point positions as adopted by the previous correlation analysis only partly reflect but cannot describe the 3-D Mars orientation with respect to the Sun. Therefore, the previously reported absence of a significant longitudinal or subsolar longitudinal dependence of the BS location does not necessarily indicate the absence of a strong influence of the crustal field. Second, the *Edberg et al.* [2009] work implies that the BS location may not be explained solely by the local crustal field strength. There is a need for investigating the potential relationship between boundary positions and the crustal magnetic field distribution over a broad surface area.

Previous observational and numerical results have been interpreted as suggesting that the Mars crustal field exerts a shielding effect by standing off the solar wind flow. However, such a simple picture is challenged by the very recent time-dependent MHD studies of *Ma et al.* [2014b] and *Fang et al.* [2015], in which the upstream solar wind is quiet and stable and the MHD equations are solved with the global crustal field continuously rotating with the planet. For the specific solar minimum case, the diurnal variation exhibits two maximums and two minimums in atmospheric loss, with the amplitude as high as $\sim$20% for O^+ and $\sim$50% for O_2^+ and CO_2^+. The variation when the strongest crustal field region rotates on the dayside is generally consistent with the shielding effect, but great ion loss perturbation of comparable amplitude also occurs when the primary crustal source rotates in the Mars wake and the dayside crustal magnetic field remains weak and quasi-static.

The latter phase of the ion loss variation is unexpected and, more importantly, opposite to the dayside shielding effect.

In a further analysis by *Fang et al.* [2015], it is revealed for the first time that the crustal field controls global atmospheric escape mainly through the combination of two simultaneously occurring processes. One of the processes, which has been widely discussed, is the dayside magnetic shielding effect that protects the Martian ionosphere/atmosphere from the penetrating solar wind and interplanetary magnetic field (IMF). There is a negative correlation, and the higher dayside crustal pressure leads to the weaker solar wind mass loading and atmospheric stripping. The other control process, which has not been revealed before, is an escape-fostering effect and manifests itself by affecting the day-night connection. The MHD results show that the cross section area of the IMB at the terminator is an excellent proxy of the effective areas of transterminator flow for all major planetary heavy ions, showing a strong positive correlation within the entire rotation period. When the strongest crustal field region rotates onto the nightside (i.e., when the dayside shielding becomes stable), there is a strong correlation in the variation pattern between the IMB cross section area and the globally integrated atmospheric loss rates. Therefore, the crustal field also plays a positive role in enhancing atmospheric erosion by regulating the boundary locations. While the dependence of the crustal field control (specifically the escape-fostering effect) on its spatial distribution is not yet quantified, these emerging more accurate, non-steady-state calculations provide a closer-to-reality view of the solar wind-Mars interaction and thus represent a promising approach to look into the near-Mars space environment in a dynamic manner. As a follow up to the work of *Fang et al.* [2015], the focus of the current study is on a quantitative understanding of

how the plasma boundaries are controlled by the crustal magnetic field so that a direct relationship can be established connecting the low-altitude crustal field distribution and globally integrated atmospheric loss.

While there are few measurements of the transterminator flow particularly at low energies at Mars (see *Franz et al.* [2010] and references therein), the transterminator ion flux at Venus [e.g., *Knudsen et al.*, 1980, 1982] has been found to be related with the ionopause location sunward of the terminator. For example, *Cravens et al.* [1982] reported that the Venusian nightside ionosphere was greatly depleted under intense solar wind dynamic pressure, and attributed to the dayside ionopause being located at lower altitudes. *Miller and Knudsen* [1987] established a statistical positive relationship for Venus between the ionopause altitude and the nightside ionospheric density, the latter of which was thought to be regulated by the plasma supply from the dayside. *Brace et al.* [1995] pointed out that the excess nightward flow at Venus in association with the elevated ionopause under low solar wind dynamic pressure may lead to greater ion escape. These Venusian findings on the terminator "nozzle" control of the day-night plasma transport [*Whitten et al.*, 1991] are similar to the Mars crustal field effect near the terminator. However, the Martian situation is much more complex than that at Venus due to the combination of the positive escape-fostering effect and the negative shielding effect from the inhomogeneous crustal field.

2. 3-D MHD Model of Mars

Our main numerical tool is the 3-D multispecies, single-fluid MHD model described by *Ma et al.* [2004] and continuously developed since then. In the present work, the same simulation case as in *Ma et al.* [2014b] and *Fang et al.* [2015] is adopted for detailed

examination. The model is configured to mimic a quiet case during 16 May 2005, when Mars was near the Northern Hemisphere autumn equinox (solar longitude L_s=211.8). Specifically, the upstream solar wind plasma is quiet and stable, with a density of 4 cm^{-3}, a velocity of 400 km/s, and thus a dynamic pressure of 1.07 nPa. The IMF follows the typical Parker spiral orientation of 56° at Mars with a magnitude of 3 nT, that is, (B_X, B_Y, B_Z)=(1.6, -2.5, 0) nT in the classic Mars-centered Solar Orbital (MSO) coordinate system. The background atmosphere and the solar EUV condition (for photoionization calculation) are appropriate for solar minimum. In the model, the intrinsic crustal field is described using the *Arkani-Hamed* [2001] model, and is updated every 4 min as the planet rotates. The Martian rotational axis is tilted with a direction of (-0.23, -0.36, 0.9) in MSO, a realistic value for 16 May 2005. The MHD model runs for 26 hours, slightly longer than one Mars rotational period, to solve the solar wind-Mars interaction in a time-dependent, non-steady-state manner. As shown in *Ma et al.* [2014b], the model results of the magnetic field (with the combination of the intrinsic crustal field and the induced field) agree well with the MGS measurements along its 12 orbits during 16 May 2005. The model-data agreement convincingly demonstrates that our time-dependent MHD model possesses a firm physical foundation for us to quantify the crustal field control, particularly from a global perspective.

A movie of the MHD results showing the dynamic interaction of the Mars system with the solar wind has been created and included in the supporting information of this paper. It is worth stressing that because of the constant impact of the solar wind and solar radiation, the perturbation in the near-Mars space environment ultimately arises from

the continuously rotating crustal field in this case study. Such the model configuration allows us to focus on the controlling effects of the Mars crustal magnetic field.

3. The Model-Derived Plasma Boundaries

As revealed by *Fang et al.* [2015], the plasma boundary locations provide important information for assessing the effects of the crustal field on global atmospheric loss. However, prior to that recent study, a simplistic axial symmetry assumption has been commonly adopted, and little is known about the actual 3-D snapshots of the boundaries. Unlike previous boundary identification, which mostly has been manually conducted along satellite tracks on a case by case basis, *Fang et al.* [2015] introduced a physics-based algorithm to automatically determine the 3-D IMB and BS locations using the gradient distribution derived from the MHD calculated plasma speed. The IMB and BS positions are obtained by scanning in the spherical and cylindrical radial directions (on the dayside and on the nightside, respectively) for peak locations of plasma speed gradients ($|\nabla U|$). To the best of our knowledge, this is the first time the 3-D structures of the boundaries at Mars are identified without adopting an axial symmetry assumption. Here we apply the algorithm to quantify the boundary locations and their dynamics during the specific quiet event.

Figure 1 shows the IMB and BS locations in the terminator plane and at the subsolar point as well as their terminator cross section areas and dayside volumes, at a cadence of 20 min (corresponding to planetary rotation of $\sim 5°$). These results are organized with respect to the longitude of the subsolar point, which continuously changes with time in an opposite direction of planetary rotation. Note that the strongest crustal field region is at about 178°E and 53°S in geographic coordinates, and the initial subsolar point at 0 UT is placed at 58.9°W and 13.0°S (refer to Figure 2 of *Fang et al.* [2015]).

We calculate the mean boundary distance in the terminator plane, $\langle R_T \rangle$, which is given by

$$\langle R_T \rangle = \frac{1}{2\pi} \int_{\varphi=0}^{2\pi} R_T(\varphi)\, \mathrm{d}\varphi, \tag{1}$$

where φ stands for the clock angle about the Sun-Mars line. R_T is the radial distance of the boundaries at X=0 as a function of φ, where the subscript 'T' means terminator. The boundary cross section area at the terminator, σ_T, which is calculated beyond the MHD inner spherical boundary by following

$$\sigma_T = \frac{1}{2} \int_{\varphi=0}^{2\pi} R_T(\varphi)^2\, \mathrm{d}\varphi \; - \pi R_0^2, \tag{2}$$

where R_0=1.03 R_M is the equivalent planetocentric distance at 100 km altitude. R_M stands for the mean Martian radius of 3396 km.

One prominent feature for both the IMB and BS is their spatial asymmetry, which dynamically changes as seen in Figure 1. Using a simple definition of $(R_{\mathrm{Tmax}} - R_{\mathrm{Tmin}})/\langle R_{\mathrm{T}} \rangle$, the overall asymmetry of the terminator distances varies between 10% and 32% for the IMB and between 4% and 14% for the BS during the planetary rotation. Because of being located at significantly lower altitudes, it is not surprising to see that the IMB is subject to more influence by the crustal magnetic field and thus exhibits a greater level of spatial asymmetry than the BS. Moreover, the asymmetry is more significant when the strongest crustal field region moves onto the dayside in comparison with that on the nightside. For instance, the boundary asymmetry is the greatest when the subsolar longitude is 228° for the IMB and 252° for the BS, respectively.

As shown in Figure 1, there are roughly double-peak responses during the specific simulation event, not only for the boundary distances and the cross section areas in the

terminator plane, but also for the bounded volumes on the dayside. The peaks occur approximately when the strongest crustal field region is close to the dawn or to the dusk. By contrast, the subsolar distances of the boundaries are displaced the most outward when the strongest field region is near noon. A straightforward inference from the different behaviors at the terminator and at the subsolar point is that the crustal field affects more efficiently the local boundary locations despite its global influence. Another important inference is that the boundaries are not rigid or easily described by geometry. They not only move but also flare and deform in a dynamic manner. Figure 1 underscores that the widely adopted axially-symmetric conic section model would miss the full complexity of the boundary shapes, and at the same time highlights our model capability of capturing the global boundary snapshots and their dynamics.

Figures 1b and 1d show pronounced north-south and dawn-dusk asymmetries in both of the boundaries. The averaged terminator distances in the Southern Hemisphere generally are greater than those in the Northern Hemisphere, which is consistent with previous observations [e.g., *Crider et al.*, 2002; *Dubinin et al.*, 2008; *Edberg et al.*, 2008]. This is almost valid no matter what orientation of the planet toward the Sun is. On the other hand, the dawn-dusk asymmetry is highly dependent on the local time of crustal magnetic anomalies. Roughly speaking, when the strongest crustal field region is on the duskside (approximately for subsolar longitude between 0° and 180°), the duskside mean distances at the terminator are greater than those on the dawnside. Vice versa occurs when the strongest crustal region is on the dawnside. Note that the dawn-dusk asymmetry is not symmetric with respect to the subsolar longitude of 180°. That is, the difference of $\langle R_T \rangle_{dusk} - \langle R_T \rangle_{dawn}$ when the subsolar longitude is less than 180° is

noticeably larger than $\langle R_T \rangle_{dawn} - \langle R_T \rangle_{dusk}$ during the other part of the rotation period. For the BS, this phenomenon may in part be explained by the dependence of the shock geometry on the upstream IMF direction. For our specific case of IMF B_X=1.6 nT and B_Y=-2.5 nT, quasi-parallel and quasi-perpendicular shocks form in the dawn and dusk sectors, respectively. It has been found that quasi-parallel shocks tend to be located at lower altitudes than quasi-perpendicular shocks [*Zhang et al.*, 1991; *Vignes et al.*, 2002; *Fang et al.*, 2015]. Another important finding in Figure 1 is that both the north-south and dawn-dusk asymmetries significantly decrease when the strongest crustal field region moves from the dayside to the nightside, which results from the reduced involvement of the crustal field in the interaction with the impinging solar wind.

The 3-D boundary results enable us to estimate the error when making an axial symmetry assumption. Our calculations show that the projected terminator distances, which are obtained by fitting the entire dayside boundary locations with conic section shapes (hereinafter denoted as R_T^{cs}), are reasonably close to the accurately calculated mean distances (i.e., $\langle R_T \rangle$ from equation (1)). The difference between R_T^{cs} and $\langle R_T \rangle$ for the IMB ranges between -0.012 R_M and 0.080 R_M during the rotation period in our specific case, with a mean of 0.020 R_M and a standard deviation of 0.019 R_M. The difference for the BS is slightly smaller, ranging between -0.030 R_M and 0.057 R_M with a mean of 0.017 R_M and a standard deviation of 0.015 R_M. However, on the other hand, R_T^{cs} is unable to describe the axially-asymmetric boundary positions $R_T(\varphi)$. The resulting percentage errors, $(R_T^{cs}\text{-}R_T(\varphi))/R_T(\varphi)$, are significant, varying between -16.5% and 19.9% for the IMB and between -7.7% and 7.5% for the BS. It is seen again that the IMB is more asymmetric than the BS.

The numerical work of *Fang et al.* [2015] shows a strong correlation between the IMB cross section area at the terminator and the effective area of transterminator flow for all major planetary heavy ions. Therefore, quantifying the terminator cross section area σ_T as well as its time variation offers a clue to inferring the variability of atmospheric loss. Undoubtedly, an accurate evaluation of σ_T relies on a detailed knowledge of the simultaneous boundary positions at the terminator $R_T(\varphi)$, which can be derived from global calculations but is unavailable for direct observations at present. σ_T is also difficult to estimate in a statistical manner. The complex and dynamically varying spatial asymmetry in the boundaries, together with significant spread in statistically obtained boundary crossing positions, make for considerable uncertainty in assessing σ_T. Nevertheless, our numerical results as presented in Figures 2a and 2b reveal the existence of a linear relationship between σ_T and $\langle R_{\text{T}} \rangle$, although the exact physics behind this relationship is unknown and needs a future study. It is suggested that we may use $\langle R_{\text{T}} \rangle$ as a proxy of σ_T in order to explore the time variation of atmospheric loss. This is practically useful because the boundary distance at the terminator (at one clock angle φ at one time) is realistically measurable or derivable through extrapolation, and therefore $\langle R_{\text{T}} \rangle$ may be statistically obtained if boundary crossings are approximately uniformly distributed in φ. In addition, Figure 2c shows that the displacement of the BS varies with the crustal field rotation in a similar phase as the IMB, which seems to conflict with the weak crustal field control of the BS as implied by previous work. We will discuss in more detail in Section 6 regarding this puzzle.

In order to quantitatively describe the crustal field control of the boundary mean distances or cross section areas in the terminator plane, it is desired to have a scalar quantity

to summarize the multi-dimensional field distribution. As discussed above, the commonly used subsolar longitude is merely a part of a location indicator and is not directly representative of the crustal field strength. A physically meaningful alternative is desired. For this purpose, we introduce a new parameter called 'scaled terminator pressure' ($P_{\rm ST}$) to represent the intrinsic crustal field intensity at 400 km altitude over a broad solar zenith angle (SZA) range. We empirically divide the crustal field distribution into 6 SZA zones and allow them to have different contributions. $P_{\rm ST}$ is assumed to follow the formula below:

$$\begin{aligned} P_{\rm ST}(t) &= \sum_{i=1}^{6} P_{{\rm ST}_i}(t) \\ &= \sum_{i=1}^{6} f_i \cdot \langle P_B(t) \rangle_i^{1/6} \end{aligned} \tag{3}$$

where t is time, i stands for one of the 6 SZA zones, and the coefficient f_i reflects their weights.

$\langle P_B \rangle_i$ in the above equation represents the normal crustal magnetic pressure averaged by area over each SZA zone, which is given by

$$\begin{aligned} \langle P_B(t) \rangle_i &= \frac{\int_{\alpha=\alpha_{i1}}^{\alpha_{i2}} \int_{\varphi=0}^{2\pi} P_B(\alpha,\varphi,t)\, sin\alpha \, {\rm d}\alpha {\rm d}\varphi}{\int_{\alpha=\alpha_{i1}}^{\alpha_{i2}} \int_{\varphi=0}^{2\pi} sin\alpha \, {\rm d}\alpha {\rm d}\varphi} \\ &= \frac{\int_{\alpha=\alpha_{i1}}^{\alpha_{i2}} \int_{\varphi=0}^{2\pi} \frac{B_0^2(\alpha,\varphi,t)}{2\mu_0} sin\alpha \, {\rm d}\alpha {\rm d}\varphi}{2\pi(cos\alpha_{i1} - cos\alpha_{i2})} \end{aligned} \tag{4}$$

where α stands for the SZA, α_{i1} and α_{i2} are the SZA limits of zone i, φ is the clock angle about the Sun-Mars line. The purpose of the integration over φ here is to average the crustal field distribution along the clock angle direction, considering that the mean distance of the boundaries is the result of the integration over φ as shown in equation (1). B_0 is the crustal magnetic field strength at 400 km altitude calculated from the *Arkani-Hamed* [2001] model. Within the context of the Mars-solar wind interaction, it is more

helpful to know the crustal field distribution in the MSO coordinate system than that in the planet-fixed geographic coordinate system. Accordingly, although the geographic distribution of the crustal field remains unchanged, its MSO distribution as a function of α and φ continuously varies with time. In addition, our preceding study of *Fang et al.* [2015] showed that using different altitudes (200 km, 400 km, or 600 km) to calculate area-averaged crustal magnetic pressure essentially made no difference in the explanation of its dayside shielding effect on ion loss.

The purpose of adding the 1/6 power to $\langle P_B \rangle_i$ in equation (3) is to make the magnetic strength approximately linearly related with the boundary height. A technical approach to represent the complex Mars crustal field distribution is to use a superposition of many dipole sources near the surface [e.g., *Purucker et al.*, 2000]. Since the strength of a dipole field drops off with radius as $1/r^3$, the magnetic pressure accordingly varies as $1/r^6$. Assuming a pressure balance across the plasma boundaries, their standoff distances are thus not linearly related to the low-altitude crustal magnetic pressure but instead tend to approximately follow the 1/6 power of the pressure. In our empirical function of P_{ST}, we take this nonlinearity into account and incorporate any necessary adjustments from the realistic crustal field distribution into the weight f_i specification. Because of the application of a 1/6 power, P_{ST} is related with but not exactly in units of pressure.

It is seen that in equation (3) there are 18 parameters to optimise: α_{i1}, α_{i2}, and f_i (i=1, ..., 6). Since no gap is assumed between the SZA zones (i.e., $\alpha_{i2} = \alpha_{(i+1)1}$), the number of the unknowns reduces to 13. To specify them, we take a brute-force approach by extensively testing a vast number of combinations of possible SZA zone divisions and weight specifications. The optimal solution is selected when the obtained $P_{\text{ST}}(t)$ has

the best time series correlation with both the IMB and BS mean terminator distances: $\langle R_{\rm T}\rangle_{\rm IMB}(t)$, $\langle R_{\rm T}\rangle_{\rm BS}(t)$. As it turns out, the SZA zones are optimally set to be 0°-15°, 15°-40°, 40°-50°, 50°-65°, 65°-90°, and 90°-130°. That is, the region where the crustal field control is considered covers the entire dayside region plus 40° past the terminator. The optimal weight for each zone is normalized with respect to the zones near the terminator: f_i=0.75, 0.20, 0.50, 0.35, 1.0, and 1.0, when i=1, ..., 6. Due to the empirical nature of this approach, the solution may not be unique. For example, increasing the number of SZA zones is expected to be helpful, which, however, is practically hard and subject to combinatorially increasing demands on computational time. Nevertheless, as long as the general format of the $P_{\rm ST}$ definition holds, our basic conclusions remain valid, which is more important than the adjustable parameter specification itself.

It is worth emphasizing that the scaled terminator pressure $P_{\rm ST}$ is solely determined by the intrinsic crustal field distribution. Whenever the Mars orientation with respect to the Sun is known and so is $B_0(\alpha, \varphi, t)$, $P_{\rm ST}$ can be calculated following equations (3) and (4). In other words, the (nearly) global crustal field distribution can be summarized into the scalar quantity at any given time.

The top panels of Figure 3 show the time variation of the calculated $P_{\rm ST}$ and its individual SZA zone components, whose relative importance is demonstrated by their percentage to the total (i.e., $P_{{\rm ST}_i}/P_{\rm ST}$, in dotted lines). It is seen that during most of the time of this specific simulation case, the combined adjacent $P_{\rm ST}$ components near the terminator (SZA 65°-90° plus 90°-130°, black line) dominate over the combination of all the other dayside components. Recalling that the main purpose of the $P_{\rm ST}$ introduction is to understand the crustal field control on the boundaries at the terminator, the domination of the

near-terminator P_{ST} components is consistent with our previous observation in Figure 1 that the crustal field is more effective in local control of the boundaries despite its global influence. Moreover, the relative importance of the P_{ST} components in different SZA zones is dynamic in nature. For instance, as the strongest crustal field region approaches noon at ~8 UT, the terminator/dayside components of P_{ST} significantly weaken/strengthen, respectively. The contribution of the terminator components to the total P_{ST} (in black dotted line) drops from ~ 60% to as low as ~ 40% at ~8 UT.

Figure 3b compares the MHD-independent P_{ST} (combination of all 6 zone components) against the model derived IMB mean distance $\langle R_T \rangle$ and cross section area σ_T at the terminator as a function of time. Their correlation is evaluated in detail through the scatter plot in Figure 3c. The achieved correlation coefficients of about 0.75 are strong and statistically significant, indicating that the empirically defined P_{ST} is a useful proxy, whose value changes closely in line with the boundary location at the terminator over time.

It should be pointed out that previous studies tended to focus on and emphasize the crustal field local effect by attempting to relate boundary locations with local magnetic anomalies. It is thus necessary to quantitatively examine whether the crustal field local control dominates or whether its global influence is equally important. In contrast with using the global crustal field distribution through P_{ST} in Figure 3c, we explore in Figure 3d the relationship between $\langle R_T \rangle$ and the local field strength explicitly. If using only the combined terminator components of P_{ST}, the correlation turns out to be very weak. We also examine a simpler and more straightforward approach by calculating the normal crustal magnetic pressure near the terminator region by substituting into equation (4)

with α_1=85° and α_2=95°, and a weak correlation is seen again. It is concluded that the crustal field has important global influence on plasma boundary locations. The strength of the local crustal field alone cannot explain the variation of the mean boundary distance at all.

In Figure 4, we extend the correlation analysis between P_{ST} and $\langle R_T \rangle$ and σ_T for the IMB to that for the BS. Note that P_{ST} only depends on the intrinsic crustal field distribution and thus remains unchanged from what has been shown in Figure 3. The correlation coefficients for the BS are slightly higher, which are 0.82. The difference in correlation coefficients may be in part due to a relatively greater uncertainty in determining the IMB than the BS from the MHD results. As demonstrated in Figure 4 of *Fang et al.* [2015], the spatial gradients of plasma quantities (such as flow speed, magnetic field magnitude, magnetic pressure, and thermal pressure) have consistent peak locations in association with BS identification. Near the IMB location, the gradient distributions are of considerable complexity, usually showing multiple peaks except for the flow speed. While it is a reasonable choice to associate the prominent peak of the flow speed gradient with the IMB location, further study is needed for uncertainty assessment.

These results provide support for and strengthen the suggestion that the shape and location of the plasma boundaries are affected by the global crustal field distribution when the external solar conditions are stable. The boundary location at the terminator is determined not only by the local crustal field but also by the distribution over the entire dayside, although different SZA zones exert different influence. This actually is expected as it makes physical sense to see that the boundary perturbation by the crustal field at the upstream propagates down the stream and affects the boundary there. From

the empirical definition of P_{ST} as shown in Figure 3a, we are able to quantitatively argue that the crustal field near the terminator region of 65°-130° in SZA is a major but not the only factor (mostly 60% but sometimes 40% in our specific case) in determining the mean terminator distance for both the IMB and BS. In addition, it should be pointed out that P_{ST}, $\langle R_T \rangle$, and σ_T are all reduced/averaged quantities. While our present work generally reveals their inherent dependence, it requires future efforts to directly connect the simultaneous 3-D imaging of the boundaries with the crustal field at low altitudes.

4. The Crustal Field Control of Global Ion Loss

The quantitative description of the crustal field control of the plasma boundaries as shown above is important for an in-depth understanding of the interaction processes at work between the solar wind and the Mars obstacle. As suggested by the recent findings of *Fang et al.* [2015], the boundary variation has an important implication for the variation of the integrated amount of tailward escaping ions. In that preceding work, we came up with an empirical function to combine the dayside and terminator control effects of the crustal field and used it to successfully predict total loss rates for all the major planetary heavy ions (O_2^+, O^+, CO_2^+). The connection was achieved by taking advantage of the IMB-bounded dayside volume. Apparently, one drawback of that empirical function is the lack of a direct connection between the loss rates and the crustal field distribution, because at that time little was known about the details of how the boundary location (specifically, IMB cross section area in the terminator plane) was controlled by the inhomogeneous crustal field. Since the gap is now filled in as seen in Figure 3c, we are ready to develop a more straightforward method to predict loss rate changes by using directly the crustal field distribution.

Prompted by *Fang et al.* [2015], we introduce a new quantity called 'scaled effective pressure' $P_{\rm Eff}$, which is defined as

$$P_{\rm Eff}(t) = -P_{\rm SD}(t - \Delta t_s) + P_{\rm ST}(t), \tag{5}$$

where $P_{\rm ST}$ is the scaled terminator pressure as described by equation (3), and $P_{\rm SD}$ is 'scaled dayside pressure' given by

$$\begin{aligned} P_{SD}(t) &= \langle P_B(t) \rangle^{1/6}_{\rm SZA<45} \\ &= \left(\frac{\int_{\alpha=0}^{\pi/4} \int_{\varphi=0}^{2\pi} \frac{B_0^2(\alpha,\varphi,t)}{2\mu_0} sin\alpha \, {\rm d}\alpha {\rm d}\varphi}{(2-\sqrt{2})\pi} \right)^{1/6} \end{aligned} \tag{6}$$

That is, $P_{\rm SD}$ is defined to be the area-averaged crustal magnetic pressure (at 400 km altitude over a relatively broad subsolar region of 0°-45° in SZA) to the power of 1/6. Due to the time lag of the dayside process in regulating global ion loss as recognized by *Fang et al.* [2015], we add a constant, species-dependent time delay Δt_s into equation (5), which has been empirically set to be Δt=0.6 h for O^+, 2.3 h for O_2^+ and CO_2^+, and 2.1 h for total heavy ions. Other than that, the definition of $P_{\rm Eff}$ is solely dependent on the intrinsic crustal field distribution in MSO and independent of our MHD model. The time-varying $P_{\rm Eff}$ and its dayside and terminator components are presented at a cadence of 4 min in the left column of Figure 5.

A few notes are made here for the $P_{\rm Eff}$ definition. First, the signs of its dayside and terminator components, $P_{\rm SD}$ and $P_{\rm ST}$, are opposite. Consistent with *Fang et al.* [2015], this reflects the underlying difference in the effects of the crustal field in different regions from a view of atmospheric loss. The dayside crustal field mainly has a shielding effect, inhibiting the extent to which the solar wind penetrates into and interacts with the upper atmosphere/ionosphere. The higher the crustal field strength confronting the solar wind

on the dayside is, the less the overlap between the solar wind and planetary neutrals becomes, and the smaller the total ion abundance that is stripped away by the solar wind is. In contrast, the terminator counterpart has an escape-fostering effect, displaying a positive correlation with ion loss. As illustrated by *Fang et al.* [2015], the IMB cross section area σ_T at the terminator is positively related with the transterminator ion flow area. Figure 3c shows that P_{ST} is an excellent proxy of σ_T and therefore its variation positively reflects somewhat the day-night connection as suggested by *Fang et al.* [2015], although the details of the physical mechanism responsible for this escape-fostering effect await further investigation.

Second, while there is no need for adding a time lag into the terminator component P_{ST}, a species-dependent time delay Δt_s has to be incorporated into the dayside component P_{SD} in order to achieve the optimal correlation analysis results as shown in the right column of Figure 5. This delay reflects the combination of two time scales during the process of atmospheric erosion. One of the time scales is associated with the response of the Mars system to the pressure imbalance caused by the rotating crustal field, including the perturbation in ionospheric composition and dynamics and in the induced magnetic field distribution. *Ma et al.* [2014a] found that under the impact of a disturbed solar wind ram pressure, unlike the near-Mars environment at high altitudes exhibiting a fast response, the low-altitude ionosphere responds quickly at the beginning but needs hours to recover to a quasi-equilibrium state. The other time scale is related with the time required for the planetary ions of the dayside origin to transport to the nightside for escape. As noted by *Fang et al.* [2015], the dayside-averaged Alfven speed in the ionosphere generally decreases with decreasing altitude to as low as about 1 km/s near the peak altitude. It is worth

emphasizing that these two time scales are involved with nonlinear physical processes, which are not isolated but interplay with each other. Consistent with these coherent pictures, we note that the time delay for O^+ is significantly shorter than that for O_2^+ and CO_2^+. This can be explained by the fact that O^+ is relatively lighter and thus dominant in abundance at higher altitudes than the other heavier ions.

Third, the crustal field distribution on the dayside has competing effects in the control of atmospheric loss as implicitly seen in equation (5). The field strength within the SZA range of 0°-45° appears in the definitions of both P_{SD} and P_{ST}. In other words, the crustal field that directly faces the impinging solar wind not only has a shielding effect of protecting the ionosphere/atmosphere from the solar wind stripping, but also exerts an escape-fostering effect by pushing the plasma boundaries farther away from the surface to facilitate ion transport to the nightside. The overall effect is the shielding effect, although the competition between these two opposite effects is dynamic in nature due to planetary rotation. We have conducted a separate MHD simulation under the identical conditions except that no crustal field is included. The results of the hypothetical calculation show greatly enhanced atmospheric loss rates if there is no crustal field protection: 1.43×10^{24}, 2.94×10^{24}, and 2.42×10^{23} per sec for O^+, O_2^+, and CO_2^+, respectively.

Figure 5 shows that the empirically defined, crustal field determined P_{Eff} is successful in describing the general trend of the time variation of globally integrated planetary ion loss. The correlation coefficients range from 0.75 to 0.82 for all the major heavy ions. These are statistically significant with extremely low p-values, considering that the data points are surveyed every 4 min over the 26-hour simulation time period. It is shown that approximately 56%-67% of the variability of total atmospheric loss can be accounted

for simply by the variability of the crustal field distribution in MSO, given that other intermediate processes (most likely nonlinear, such as ionospheric and induced magnetic field feedback) are not explicitly included in the correlation analysis.

5. Comparison with MAVEN Observations

The main purpose of this section is to test our empirically derived, physics-based algorithm with the observations from NASA Mars Atmosphere and Volatile EvolutioN mission (MAVEN) [*Jakosky et al.*, 2015]. Because of the difficulty in evaluating atmospheric loss and its variability at a short time scale, we focus our model-data comparison on plasma boundary locations at the terminator. In this study, we compare our MHD-derived prediction with the MAVEN-observed variability of the BS but not the IMB, due to the following considerations. First, there is significant uncertainty in defining the lower boundary of the magnetosheath, and the relationship between the IMB and MPB remains poorly understood. Second, sometimes there is an ambiguity in our numerical identification of the IMB near the subsolar region (see Figure 4 of *Fang et al.* [2015], and the discussions in the text). Third, the recent MAVEN observation from J. Gruesbeck et al. (Martian-solar wind interaction boundaries as observed by MAVEN, paper presented at 2015 American Geophysical Union Fall Meeting, San Francisco, California, 2015) suggests that the MPB has a significant thickness comparable to or even larger than that of the BS. Therefore, The relative error in comparing the IMB/MPB location becomes significantly higher than for the BS.

In this work, we adopt the MAVEN-observed BS locations by *Masunaga et al.* [2016], which have been manually identified by examining ion energy spectra from the Solar Wind Ion Analyzer (SWIA) instrument [*Halekas et al.*, 2015] and magnetic field measurements

from the magnetometer (MAG) instrument [*Connerney et al.*, 2015]. The boundary crossing is determined to be associated with a shocked solar wind from upstream conditions together with intensified magnetic field strength and disturbance [see *Masunaga et al.*, 2016]. The data coverage starts from the early phase of MAVEN science operations on November 2014 through April 2016.

Figure 6 shows the MAVEN BS crossing in the aberrated, classic MSO and Mars-Solar-Electric field (MSE) coordinate systems. The convection electric field direction, which is needed for the transformation to MSE coordinates, is estimated using the IMF measured by MAG and averaged on an orbit-by-orbit basis. Each boundary crossing position is color coded by the corresponding SWIA-measured, orbit-averaged solar wind dynamic pressure upstream of the BS [*Halekas et al.*, 2017]. The data shown in the left column are organized in cylindrical coordinates relative to the Mars-Sun line, and the right column shows the locations after being projected to the terminator plane under a conic section shape assumption: $r = L/(1 + \epsilon \cos\theta)$. L is the semi-latus rectum, ϵ is the eccentricity. Polar coordinates (r, θ) are the distance and angle determined with respect to the focus at the Mars-Sun line at $X = X_0$.

To describe the average BS shape, we consider only the crossings on the dayside: X$\geq$-0.1 R_M and SZA $\geq 5°$. The data exclusion is made to prevent the probable bias due to the limitation in the MAVEN orbital coverage as seen in Figure 6a/6c. The results of our conic section fit are X_0=0.42 R_M, L=2.303 R_M, and ϵ=0.872. As shown in Figure 6, the fit to the MAVEN data on the dayside is remarkably close to that of *Vignes et al.* [2000], which is based on MGS observations. Because our averaged BS shape is less flared

(comparing to ϵ=1.03 for the BS by *Vignes et al.* [2000]), the discrepancy between the two empirical fits gradually becomes significant down the tail.

In Figure 6b, the north-south asymmetry is pronounced in the mean BS terminator distance, which is obtained by extrapolating the MAVEN data points using the new conic section fit (by adjusting L values with X_0 and ϵ fixed). The distance in the MSO Southern Hemisphere is located farther by 0.14 R_M on average, which is significant in statistics according to Student's t-test. While not directly comparable, this observed difference is reasonably consistent with the model results in Figure 1d (compare blue and red lines). The asymmetry is often attributed to the fact that the crustal field in the Southern Hemisphere is significantly stronger. There are a few other factors that may also contribute to this difference in the data, including limited spatial coverage and unconstrained solar wind and solar EUV conditions.

After being organized in the MSE coordinate system in Figure 6d, the data points basically are uniformly distributed in the terminator plane. To ensure a meaningful and reasonable model-data comparison at X=0, we limit usable data points to those having comparable external conditions when the solar wind dynamic pressure deviates from the model input of 1.07 nPa by less than 0.5 nPa. In addition, we neglect the data points on the nightside (X<-0.1 R_M) and over the subsolar region (SZA $< 5°$) in order to make extrapolation bias and errors, respectively, as low as possible. The final data points suitable for comparison are shown in Figures 6e and 6f, where the seemly reverse north-south asymmetry (actually in the convection electric field direction in MSE) in the averaged R_T is statistically insignificant according to Student's t-test.

Figure 7 shows the reorganization of the MAVEN-derived BS distance to the Mars-Sun line in the terminator plane (as in Figure 6f), in terms of the empirical parameter of P_{ST} (as defined in equations (3) and (4)). It is stressed that our empirical results are limited to predicting the general control of the crustal field. It is the averaged terminator distance ($\langle R_T \rangle$, scalar) but not the simultaneous positions in the terminator plane ($R_T(\varphi)$, 1-D matrix) that can be empirically related with P_{ST} at present. Therefore, we have to statistically derive mean boundary distances from these single point measurements, which are scattered over the terminator plane, before a meaningful comparison can be made.

While scattering over a wide P_{ST} range, the data points are significantly concentrated at higher values. To ensure a reasonable statistics, we sort the 936 data points into two groups. For the dense data points at $P_{ST} \geq 2.5$, we divide them into 10 uniformly distributed fine bins, within which the number of data points is overall satisfactory. For the sparse data points at $P_{ST} < 2.5$, we use 5 coarse bins to organize the data. The MAVEN sparse coverage at the low P_{ST} values prevents us from deriving a statistically convincing conclusion, but is still useful to demonstrate a general trend of $\langle R_T \rangle$ with respect to P_{ST}. By eyeballing the figure, we can see a trend change from a flat slope in the low P_{ST} part to a significantly inclined slope approximately when P_{ST} is greater than 2.5. In what follows, we will make a quantitative comparison of the observations against the model results.

We apply two ways to derive $\langle R_T \rangle$ values from single R_T measurements to facilitate a direct comparison. The first approach is to calculate arithmetic means within each of the P_{ST} bins, as marked by red diamonds in the figure. The validity of this procedure is based on the assumption that the data points in a bin are adequately representative of the 1-D $R_T(\varphi)$ distribution. A careful examination (not presented here) shows that

the data points are approximately uniformly scattered on the $Y-Z$ plane within each of these coarse and fine bins. The second method of calculating the mean is to further divide the data points within a bin into eight 45°-clock angle sectors on the $Y-Z$ plane, calculate the median value within each sector, and then obtain the arithmetic average of these medians. The purpose of this method is to eliminate possible bias resulting from nonuniform clustering of the data points in clock angle φ. The results are indicated by the blue circles in Figure 7. It is seen that these two approaches yield close results, supporting that the data points within the P_{ST} bins widely spread in clock angle after being transformed from MSO to the more physically meaningful MSE and thus are well representative of $R_T(\varphi)$.

In Figure 7, we perform a linear fit to the mean values that are derived from the MAVEN observations, separately for the data points with P_{ST} values lower or higher than 2.5. These experimental $P_{ST}-\langle R_T\rangle$ relationships, shown in red/blue lines, can be directly compared with the model prediction in dashed green line (as previously shown by the blue line in Figure 4b). It should be pointed out that the model results are obtained from a specific simulation case, in which P_{ST} varies within a limited range. Therefore, we limit the model-data comparison to the high P_{ST} part. A quick glance shows that the red/blue solid lines and the green dashed line are significantly separated. Nevertheless, it has been noted that the solar radiation condition when the MAVEN measurements were made differs from what is used in the numerical simulation. In this study, we choose to compare the $F_{10.7}$ solar radio flux rather than to use the dedicated solar radiation measurement from the MAVEN Extreme Ultraviolet Monitor (EUVM) [*Eparvier et al.*, 2015]. There are a few considerations for this choice. First, it is the $F_{10.7}$ index that the

MHD model currently uses to specify the photoionization rate. For the specific simulation case under solar minimum, the scaled $F_{10.7}$ at Mars has been set to be 38.8. Second, the statistical study of *Edberg et al.* [2009], which quantifies the impact of solar radiation on boundary locations, uses $F_{10.7}$ as the proxy of solar EUV. Therefore, it is $F_{10.7}$ rather than sophisticated MAVEN/EUVM data products that serves to facilitate model-data comparisons.

To estimate the $F_{10.7}$ intensity for the MAVEN observations, we extrapolate the Earth-based index to the Mars orbit by considering solar radiation decrease in the heliocentric distance as well as the angular separation between Earth and Mars [e.g., *Thiemann et al.*, 2016]. The solar radiation flux is assumed to fall off by the $1/d^2$ law, where d is the distance from the Sun. Using the difference in heliocentric longitude between the two planets, the $F_{10.7}$ value is shifted in time to take into account the solar rotation change. After making these two adjustments on a point-by-point basis, we obtain the scaled $F_{10.7}$ values associated with the MAVEN data points used in Figure 7, which have a mean value of $\langle F_{10.7} \rangle$=55.7 at Mars. Substituting the $F_{10.7}$ numbers (38.8/55.7 for the model/observation, respectively) into the empirical relationship as in Figure 10a of *Edberg et al.* [2009], we would roughly expect an average 9% enhancement on the model-calculated BS terminator distance if the model solar EUV input were enhanced to the same level as in the MAVEN observations. The adjusted model prediction is shown in solid green line in Figure 7.

In light of the considerations discussed above, we are ready to make comparisons in Figure 7 more appropriately between the solid green line from the model and the solid red/blue lines (not single data points) from MAVEN. As can be seen, these results are

in reasonably good agreement. Many factors need to be considered to understand or interpret the model-data discrepancy. For example, the model results are obtained for a specific quiet solar wind event with a fixed subsolar latitude, while the observations include a variety of external conditions and crustal field orientation (including subsolar longitude/latitude) conditions. Moreover, the boundary dependence on solar EUV or $F_{10.7}$ is still not well understood. In addition, our model calculated $\langle R_T \rangle$ is the average over the 1-D distribution of $R_T(\varphi)$ exactly in the terminator plane. By contrast, the MAVEN $\langle R_T \rangle$ observations include many dayside boundary crossings through projection to the terminator plane by assuming a single conic section shape, which is a procedure commonly used to increase statistics. The statistics will be improved when more MAVEN data are available near the terminator as the mission goes on and/or other mission measurements (like Mars Express) are added.

For P_{ST} values lower than 2.5, although our current numerical work does not cover this parameter range, the observation of the MAVEN results in Figure 7 suggests that $\langle R_T \rangle$ is almost unaffected by P_{ST}. While it is questionable whether the statistics for these low P_{ST} value data suffices, it makes physical sense to see a flat slope when the crustal field control is weak and then an inclined slope after a threshold is reached. If such a picture is real, it suggests that when the crustal field is weak (in terms of the control on terminator boundary locations), the plasma boundary is mainly maintained by the other processes like the ionosphere and the induced magnetic field. The influence of the intrinsic crustal field gradually increases and becomes important or even dominant only after P_{ST} is beyond a threshold value of $\sim$2.5. The black curve in Figure 7 shows an exponential fit to all the mean data points, illustrating a nonlinear relationship of $\langle R_T \rangle$ over a broad P_{ST} range.

6. Discussion

Our time-dependent MHD simulation results as shown in Section 3 illustrate that the crustal field controls the shape and location of the plasma boundaries on a global scale, for not only the IMB but also the BS. Both boundaries significantly respond to the continuous rotation of Mars intrinsic crustal magnetic anomalies, even if the external drivers (i.e., solar wind and solar EUV) remain unchanged. It is argued that the location of a single point at the planet, including the widely used subsolar longitude, is incapable of representing the multidimensional spatial distribution of the crustal field. This has motivated us to develop the empirical parameter of P_{ST} to connect the crustal field distribution with boundary locations.

There seems at first glance to be an inconsistency between our findings and previous data analysis. Our results clearly demonstrate the crustal field control, since the external driving is static in our simulation setup. However, the earlier data analyses [*Slavin et al.*, 1991; *Vignes et al.*, 2002; *Mazelle et al.*, 2004; *Edberg et al.*, 2008, 2009; *Halekas et al.*, 2017] had a different implication. By using longitudinal or subsolar longitudinal locations to organize boundary distances, the early works found no compelling evidence that the BS location had a discernible dependence on the crustal field distribution at low altitudes. To solve this puzzle, we adopt the same data organization technique and have the MAVEN results in Figure 8. Our observation is consistent with previous findings that the BS is located farther away from the surface in the Southern Hemisphere than that in the Northern Hemisphere, but its dependence on subsolar longitude is indeed not apparent.

Actually, the inconsistency issue is not as real as it seems. Previous observations and ours in Figure 8 agree on a weak dependence on subsolar longitude. However, it would

be problematic to further infer that there is a weak dependence of the BS location on the crustal field orientation with respect to the Sun. This is because although subsolar longitude is suitable for being a quick indicator of the crustal field position, it does not include all the needed information to fairly place the global crustal field distribution within the Mars-solar wind interaction. For instance, subsolar latitude provides the complementary information of the subsolar point position, and equally importantly determines the crustal field distribution as a function of SZA. The SZA distribution of the crustal field, as suggested by our results in Figure 3 and Figure 4, is the key determinant of boundary locations. The reason why we see strong crustal field control in Figure 1 and weak dependence on subsolar longitude in Figure 8 at the same time can be explained as follows. The statistical analysis in Figure 8 spans a broad time range including many seasons, which means that the subsolar latitude associated with the data points within a subsolar longitude bin may be significantly different. Note that the subsolar latitude in our numerical simulation case is essentially fixed over one Mars rotation. As a consequence, it is the mixing result that the statistical data organization as in previous studies and in Figure 8 actually demonstrates by including different crustal field controlling effects in response to a variety of subsolar longitude-latitude configurations.

It has been shown in Figures 3 and 4 that the entire dayside region plus 40° past the terminator are responsible for the plasma boundaries at the terminator (i.e., $\langle R_T \rangle$ and σ_T), although the local region (65°-130° in SZA) generally has more influence than the dayside SZA zones. The weights f_i in our empirical P_{ST} definition demonstrate a complex, non-monotonous dependence on SZA. The irregular weight distribution can be due to several reasons. First, the boundaries at lower SZAs generally located at lower

altitudes, becoming more susceptible to the crustal field. On the other hand, the solar wind dynamic pressure along the normal boundary direction generally increases with decreasing SZA. The sensitivity of the boundary height to the perturbation in the local crustal field strength reflects this competition. Second, it is the terminator distance that we currently focus on, which means that the weights have implicitly included the projection effect from the dayside to the terminator. If a conic section shape is a reasonable first-order approximation (as shown in Figure 6), then a height shift of the boundaries at a lower SZA would result in a greater shift at the terminator because of the SZA dependence of the slope. All of these factors work together and ultimately make the SZA dependence of the crustal field influence complicated.

In order to reasonably compare MAVEN measurements with our model prediction, we have constrained external solar wind conditions to have a comparable dynamic pressure $P_{\rm dyn}$. The solar EUV effect has also been taken into account in our comparison. Besides $P_{\rm dyn}$, the magnetosonic Mach number $M_{\rm MS}$ is another solar wind parameter that may significantly affect the BS position [e.g., *Edberg et al.*, 2009; *Halekas et al.*, 2017]. In this study, we choose to use $P_{\rm dyn}$ rather than $M_{\rm MS}$ to constrain the MAVEN data. One reason is that $P_{\rm dyn}$ has been more widely considered and used in the Mars science community because of its relatively greater availability. For example, the Mars Express spacecraft is not equipped with a magnetometer. By using the commonly adopted parameter, our study is placed in a wider context and thus facilitates comparisons by future studies. Another reason is that, the estimation of $M_{\rm MS}$ requires additional knowledge of the IMF and the solar wind ion and electron temperatures. While the IMF is directly measured by the MAVEN MAG instrument, plasma temperature derivation has to be involved with

many assumptions. By including extra data sets and associated errors and uncertainties, using $M_{\rm MS}$ does not necessarily lead to a more accurate analysis than using $P_{\rm dyn}$ in reality.

We realize that in order to have adequate MAVEN data points for the statistical analysis in Figure 7, the solar wind $P_{\rm dyn}$ is constrained to a finite range between 0.57 and 1.57 nPa. The variability together with other factors (including solar EUV, solar wind $M_{\rm MS}$, spatial asymmetry of the BS) contribute to significant scatter of the data points in terms of R_T. Nevertheless, the general trend of the $P_{\rm ST} - \langle R_T \rangle$ relationship, particularly the inclined slope when $P_{\rm ST} \geq$2.5, is believable for a couple of reasons. First, if the slope were not real but mainly caused by the solar wind dynamic pressure or solar EUV, then there would be a significant data bias that favors a lower $P_{\rm dyn}$ or a greater EUV flux for those data points with a larger $P_{\rm ST}$ value. Our data examination has ruled out the possibility of such a bias. Second, according to the empirical study of *Edberg et al.* [2009], the solar wind $P_{\rm dyn}$ values of 0.57 and 1.57 nPa may cause a difference of 0.04 R_M in R_T on average. This uncertainty is too small to account for the $\sim$0.3 R_M difference in $\langle R_T \rangle$ between $P_{\rm ST}$=2.5 and 2.8.

The crustal field distribution in this work is characterized by adopting the *Arkani-Hamed* [2001] model, whose results at some places may deviate from MGS observations [*Cain et al.*, 2003]. It awaits future study to assess how the error/uncertainty with the crustal field model affects our quantitative analysis. Nevertheless, our basic conclusions are expected to remain valid, considering the satisfactory reproduction of the magnetic field vector along the MGS orbits as demonstrated by *Ma et al.* [2014b].

The importance of the continuously rotating crustal field is convincingly illustrated when external drivers are static. While not explicitly included in our empirical study,

the other physical processes at work have been self-consistently included in our numerical simulation of the Mars-solar wind interaction. For example, the ionosphere is continuously perturbed on its dynamics, composition, and current system. The induced magnetic field also dynamically changes. These intermediate processes are nonlinear and hard to be quantitatively included in empirical formulae. Our results show that the intrinsic crustal field change in MSO itself is important enough to account for the majority of the variability ($56\% - 67\%$) in the mean boundary distances (Figures 3 and 4) and in total planetary ion loss rates (Figure 5). It should be stressed that our empirical models are derived and validated under specific external (solar wind plasma, IMF, and solar EUV) and internal (subsolar latitude) conditions. While the results are expected to represent the general control of the crustal field, future work is required to investigate in more detail how the crustal field control varies within these parameter space.

7. Summary and Conclusion

We apply a time-dependent MHD simulation to investigate the 3-D Mars BS and IMB and planetary ion loss as well as their dynamic changes with time. By applying the newly developed 3-D boundary identification algorithm of *Fang et al.* [2015], we examine the spatial asymmetry of the boundaries, with a focus on the terminator plane. It is found that significant spatial asymmetry occurs. Our model confirms the well-expected hemispheric asymmetry: the BS and IMB in the Southern Hemisphere are generally displaced at a higher altitude due to the presence of significantly stronger crustal field regions. The degree of the asymmetry is dynamic and generally stronger when the strongest crustal field region rotates onto the dayside.

Our results illustrate that the Mars crustal magnetic field has a clear and significant influence on not only the IMB (which is consistent with previous studies) but also the BS (which was unclear from previous work). Our detailed analysis suggests that widely used subsolar longitude of the planet is insufficient for indicating the relative position of the global crustal field distribution with respect to the Sun. Subsolar latitude provides complementary information that is equally important for understanding the Mars-solar wind interaction. Although all the studies to date (including our MAVEN data analysis in this work) found no significant dependence of the BS distance on subsolar longitude, this does not imply that the BS is not significantly influenced by the crustal field. Instead, our analysis has convincingly revealed the inherent controlling effect of the crustal field, which simply does not manifest itself by organizing data in terms of subsolar longitude. It is argued that using a local quantity like subsolar longitude would result in an indiscernible/weak dependence showing up due to the mix of different subsolar latitude scenarios, given that the subsolar latitude periodically migrates with season.

It is thus desired to have a physically meaningful parameter to represent the global crustal field distribution. For this purpose, we brute force search over the model results and introduce an empirical quantity called 'scaled terminator pressure' $P_{\rm ST}$. We divide the dayside region at 400 km altitudes into 6 zones in terms of SZA within the range of 0°-130°, calculate the 1/6 power of the area-averaged crustal magnetic pressure for each zone, and then sum them up using appropriate weighting factors. It is demonstrated that the time variation of $P_{\rm ST}$ is closely correlated with the mean distances $\langle R_T \rangle$ and the cross section areas σ_T for both the IMB and the BS in the terminator plane. The empirical formula of $P_{\rm ST}$ suggests that the crustal field near the terminator region is a

major but not the only factor in determining the aforementioned terminator quantities. The crustal field distribution within the SZA of 65°-130° generally accounts for ∼60% of P_{ST} in the specific simulation case. The percentage may drop to ∼40% when the strongest crustal field region moves close to the subsolar region. This implies that the crustal field affects more the local boundary locations, despite its global influence. The model-derived $P_{ST} - \langle R_T \rangle$ relationship is further verified by comparison with MAVEN observations. It is found that the $P_{ST} - \langle R_T \rangle$ relationship over a wide P_{ST} is actually nonlinear. The influence of the intrinsic crustal field gradually increases and becomes important or even dominant only after P_{ST} is beyond a threshold value.

Finally, following *Fang et al.* [2015], we introduce another empirical quantity called 'scaled effective pressure' P_{Eff}, which consists of two components. The terminator component is P_{ST}, and the dayside component has a negative sign and is calculated using the crustal field distribution over a broad subsolar region of 0°-45° in SZA. Furthermore, the dayside component is associated with a significant time lag when compared with ion loss: 0.6 h for O^+, 2.3 h for O_2^+ and CO_2^+, and 2.1 h for total ion loss. Our empirically defined P_{Eff}, which is solely dependent on the crustal field distribution, accounts for $56\% - 67\%$ variability of the globally integrated ion loss rates. All together, it is suggested that the crustal field has two competing effects in controlling ion loss. One is the shielding effect from the field on the dayside. The other is the escape-fostering effect from the field over the entire dayside plus 40° past the terminator. The shielding effect negatively controls the solar wind penetration, mass loading, and thus atmospheric stripping. The escape-fostering effect positively affects the transterminator ion flow area and thus day-night connection, although the underlying mechanism remains to be determined. These two

effects coexist and compete with each other in finally controlling the time variation of atmospheric erosion.

Acknowledgments. The work was supported by the NASA Mars Atmosphere and Volatile EvolutioN (MAVEN) project through the Mars Exploration Program. Resources supporting the MHD simulations and analyses were provided by the NASA High-End Computing Program through the NASA Advanced Supercomputing Division at Ames Research Center. All MAVEN data are publicly available through the NASA Planetary Data System. We acknowledge the OMNIWEB service by NASA for access to solar $F_{10.7}$ data. X. Fang would like to thank E. Thiemann for a helpful discussion regarding $F_{10.7}$ extrapolation from Earth to Mars. For the distribution of the model results used in this study, please contact the corresponding author.

References

Acuna, M. H., et al. (1998), Magnetic field and plasma observations at Mars: Initial results of the Mars Global Surveyor mission, *Science, 279*, 1676.

Andrews, D. J., L. Andersson, G. T. Delory, R. E. Ergun, A. I. Eriksson, C. M. Fowler, T. McEnulty, M. W. Morooka, T. Weber, and B. M. Jakosky (2015), Ionospheric plasma density variations observed at Mars by MAVEN/LPW, *Geophys. Res. Lett., 42*, 8862-8869, doi:10.1002/2015GL065241.

Arkani-Hamed, J. (2001), A 50-degree spherical harmonic model of the magnetic field of Mars, *J. Geophys. Res., 106*, 23,197.

Brain, D. A., J. S. Halekas, R. Lillis, D. L. Mitchell, R. P. Lin, and D. H. Crider (2005), Variability of the altitude of the Martian sheath, *Geophys. Res. Lett., 32*, L18203,

doi:10.1029/2005GL023126.

Brace, L. H., R. E. Hartle, and R. F. Theis (1995), The nightward ion flow scenario at Venus revisited, *Adv. Space Res., 16*, 99-112, doi:10.1016/0273-1177(95)00255-D.

Brain, D. A., A. H. Baker, J. Briggs, J. P. Eastwood, J. S. Halekas, and T.-D. Phan (2010), Episodic detachment of Martian crustal magnetic fields leading to bulk atmospheric plasma escape, *Geophys. Res. Lett., 37*, L14108, doi:10.1029/2010GL043916.

Brecht, S. H., and S. A. Ledvina (2014), The role of the Martian crustal magnetic fields in controlling ionospheric loss, *Geophys. Res. Lett., 41*, 5340-5346, doi:10.1002/2014GL060841.

Cain, J. C., B. B. Ferguson, and D. Mozzoni (2003), An n = 90 internal potential function of the Martian crustal magnetic field, *J. Geophys. Res., 108*, 5008, doi:10.1029/2000JE001487, E2.

Connerney, J. E. P., J. R. Espley, P. Lawton, S. Murphy, J. 496 Odom, R. Oliversen, and D. Sheppard (2015), The maven magnetic field investigation, *Space Sci. Rev.*, 1-35, doi:10.1007/s11214-015-0169-4.

Cravens, T., L. Brace, H. Taylor Jr., S. Quenon, C. Russell, W. Knudsen, K. Miller, A. Barnes, J. Mihalov, and F. Scarf (1982), Disappearing ionospheres on the nightside of Venus, *Icarus, 51*, 271-282, doi:10.1016/0019-1035(82)90083-5.

Crider, D. H., M. S. Acuna, J. E. P. Connerney, D. Vignes, N. F. Ness, A. M. Krymskii, T. K. Breus, H. Reme, C. Mazelle, D. L. Mitchell, R. P. Lin, P. A. Cloutier, and D. Winterhalter (2002), Observations of the latitude dependence of the location of the martian magnetic pileup boundary, *Geophys. Res. Lett., 29(8)*, doi:10.1029/2001GL013860.

Dong, C., S. W. Bougher, Y. Ma, G. Toth, Y. Lee, A. F. Nagy, V. Tenishev, D. J. Pawlowski, M. R. Combi, and D. Najib (2015), Solar wind interaction with the Martian upper atmosphere: Crustal field orientation, solar cycle, and seasonal variations, *J. Geophys. Res. Space Physics, 120*, 7857-7872, doi:10.1002/2015JA020990.

Dubinin, E., M. Fraenz, J. Woch, E. Roussos, J. D. Winningham, R. A. Frahm, A. Coates, F. Leblanc, R. Lundin, and S. Barabash (2008), Access of solar wind electrons into the Martian magnetosphere, *Ann. Geophys., 26*(11), 3511-3524, doi:10.5194/angeo-26-3511-2008.

Dubinin, E., M. Fraenz, D. Andrews, and D. Morgan (2016), Martian ionosphere observed by Mars Express. 1. Influence of the crustal magnetic fields, *Planet. Space Sci., 124*, 62-75, doi: 10.1016/j.pss.2016.02.004.

Edberg, N., M. Lester, S. Cowley, and A. Eriksson (2008), Statistical analysis of the location of the Martian magnetic pileup boundary and bow shock and the influence of crustal magnetic fields, *J. Geophys. Res., 113*, A08206, doi:10.1029/2008JA013096.

Edberg, N., D. Brain, M. Lester, S. Cowley, R. Modolo, M. Franz, and S. Barabash (2009), Plasma boundary variability at Mars as observed by Mars Global Surveyor and Mars Express, *Ann. Geophys., 27*, 3537.

Edberg, N. J. T., M. Lester, S. W. H. Cowley, D. A. Brain, M. Frnz, and S. Barabash (2010), Magnetosonic Mach number effect of the position of the bow shock at Mars in comparison to Venus, *J. Geophys. Res., 115*, A07203, doi:10.1029/2009JA014998.

Eparvier, F. G., P. C. Chamberlin, T. N. Woods, and E. M. B. Thiemann (2015), The solar extreme ultraviolet monitor for MAVEN, *Space Sci. Rev.*, 1-9, doi:10.1007/s11214-015-0195-2.

Fang, X., M. W. Liemohn, A. F. Nagy, J. G. Luhmann, and Y. Ma (2010a), On the effect of the martian crustal magnetic field on atmospheric erosion, *Icarus, 206*, 130-138, doi:10.1016/j.icarus.2009.01.012.

Fang, X., M. W. Liemohn, A. F. Nagy, J. G. Luhmann, and Y. Ma (2010b), Escape probability of Martian atmospheric ions: Controlling effects of the electromagnetic fields, *J. Geophys. Res., 115*, A04308, doi:10.1029/2009JA014929.

Fang, X., Y. Ma, D. Brain, Y. Dong, and R. Lillis (2015), Control of Mars global atmospheric loss by the continuous rotation of the crustal magnetic field: A time-dependent MHD study, *J. Geophys. Res. Space Physics, 120*, 10,926-10,944, doi:10.1002/2015JA021605.

Franz, M., E. Dubinin, E. Nielsen, J. Woch, S. Barabash, R. Lundin, and A. Fedorov (2010), Transterminator ion ow in the Martian ionosphere, *Planet. Space Sci. , 58*(1), 14421454, doi:10.1016/j.pss.2010.06.009.

Gurnett, D. A., et al. (2005), Radar soundings of the ionosphere of Mars, *Science, 310*, 19291933, doi:10.1126/science.1121868.

Halekas, J., E. Taylor, G. Dalton, G. Johnson, D. Curtis, J. McFadden, D. Mitchell, R. Lin, and B. Jakosky (2015), The solar wind ion analyzer for maven, *Space Sci. Rev., 195*, 125-151, doi:10.1007/s11214-013-0029-z.

Halekas, J. S., et al. (2017), Structure, dynamics, and seasonal variability of the mars-solar wind interaction: MAVEN solar wind ion analyzer inflight performance and science results, *J. Geophys. Res. Space Physics, 122*, 547-578, doi:10.1002/2016JA023167.

Hara,T.,K.Seki,H.Hasegawa,D.A.Brain, K. Matsunaga, and M. H. Saito (2014), The spatial structure of Martian magnetic flux ropes recoveredby the Grad-

Shafranov reconstruc-tion technique, *J. Geophys. Res.Space Physics, 119*, 1262-1271,doi:10.1002/2013JA019414.

Jakosky, B., et al. (2015), The Mars atmosphere and volatile evolution (MAVEN) mission, *Space Sci. Rev.*, 1-46, doi:10.1007/s11214-015-0139-x.

Knudsen, W. C., K. Spenner, K. L. Miller, and V. Novak (1980), Transport of ionospheric O+ ions across the Venus terminator and implications, *J. Geophys. Res., 85*(A13), 78037810, doi:10.1029/JA085iA13p07803.

Knudsen, W. C., Banks, P. M. and Miller, K. L. (1982), A new concept of plasma motion and planetary magnetic field for Venus, *Geophys. Res. Lett., 9*, 765768.

Krymskii, A. M., N. F. Ness, D. H. Crider, T. K. Breus, M. H. Acuna, and D. P. Hinson (2004), Solar wind interaction with the ionosphere/atmosphere and crustal magnetic fields at Mars: Mars Global Surveyor Magnetometer/Electron Reflectometer, radio science, and accelerometer data, *J. Geophys. Res., 109*, A11306, doi:10.1029/2004JA010420.

Ma, Y., A. F. Nagy, I.V. Sokolov, and K. C. Hansen (2004), Three-dimensional, multispecies, high spatial resolution MHD studies of the solar wind interaction with Mars, *J. Geophys. Res., 109*, A07211, doi:10.1029/2003JA010367.

Ma, Y. J., X. Fang, A. F. Nagy, C. T. Russell, and G. Toth (2014a), Martian ionospheric responses to dynamic pressure enhancements in the solar wind, *J. Geophys. Res. Space Physics, 119*, 1272-1286, doi:10.1002/2013JA019402.

Ma, Y., X. Fang, C. T. Russell, A. F. Nagy, G. Toth, J. G. Luhmann, D. A. Brain, and C. Dong (2014b), Effects of crustal field rotation on the solar wind plasma interaction with Mars, *Geophys. Res. Lett., 41*, doi:10.1002/2014GL060785.

Masunaga, K., K. Seki, D. A. Brain, X. Fang, Y. Dong, B. M. Jakosky, J. P. McFadden, J. S. Halekas, and J. E. P. Connerney (2016), O+ ion beams reflected below the Martian bow shock: MAVEN observations, *J. Geophys. Res. Space Physics, 121*, doi:10.1002/2016JA022465.

Mazelle, C., et al. (2004), Bow shock and upstream phenomena at Mars, *Space Sci. Rev.*, 111, 115-181.

Miller, K. L., and W. C. Knudsen (1987), Spatial and temporal variations of the ion velocity measured in the Venus ionosphere, *Adv. Space Res., 7*, 107110.

Nilsson, H., N. J. T. Edberg, G. Stenberg, S. Barabash, Y. Futaana, M. Holmstrom, R. Lundin, and A. Fedorov (2011), Total heavy ion escape from Mars and influence from solar wind conditions and crustal magnetic fields, *Icarus*, doi:10.1016/j.icarus.2011.08.003.

Purucker, M., D. Ravat, H. Frey, C. Voorhies, T. Sabaka, and M. Acuna (2000), An altitude-normalized magnetic map of Mars and its interpretation, *Geophys. Res. Lett., 27*(16), 2449-2452, doi:10.1029/2000GL000072.

Slavin, J. A., K. Schwingenschuh, W. Riedler, and Y. Yeroshenko (1991), The solar wind interaction with Mars: Mariner 4, Mars 2, Mars 3, Mars 5, and Phobos 2 observations of bow shock position and shape, *J. Geophys. Res., 96*(A7), 11235-11241, doi:10.1029/91JA00439.

Thiemann, E., P. Chamberlin, F. Eparvier, T. Woods, S. Bougher, and B. Jakosky (2016), The MAVEN EUVM level 3 spectral irradiance model: Algorithms and results, *J. Geophys. Res. Space Physics, 121*, this issue.

Vignes, D., et al. (2000), The solar wind interaction with Mars: Locations and shapes of the bow shock and the magnetic pile-up boundary from the observations of the

MAG/ER Experiment onboard Mars Global Surveyor, *Geophys. Res. Lett., 27(1)*, 49-52, doi:10.1029/1999GL010703.

Vignes, D., M. H. Acuna, J. E. P. Connerney, D. H. Crider, H. Reme, and C. Mazelle (2002), Factors controlling the location of the Bow Shock at Mars, *Geophys. Res. Lett., 29(9)*, doi:10.1029/2001GL014513.

Whitten, R. C., A. Barnes, and P. T. McCormick (1991), Plasma motions in the Venus ionosphere: Transition to supersonic flow, *J. Geophys. Res., 96*, 11,057.

Withers, P. (2009), A review of observed variability in the dayside ionosphere of Mars, *Adv. Space Res., 44*, 277-307.

Zhang, T., K. Schwingenschuh, C. T. Russell, and J. G. Luhmann (1991), Asymmetries in the location of the Venus and Mars bow shock, *Geophys. Res. Lett., 18*(2), 127-129, doi:10.1029/90GL02723.

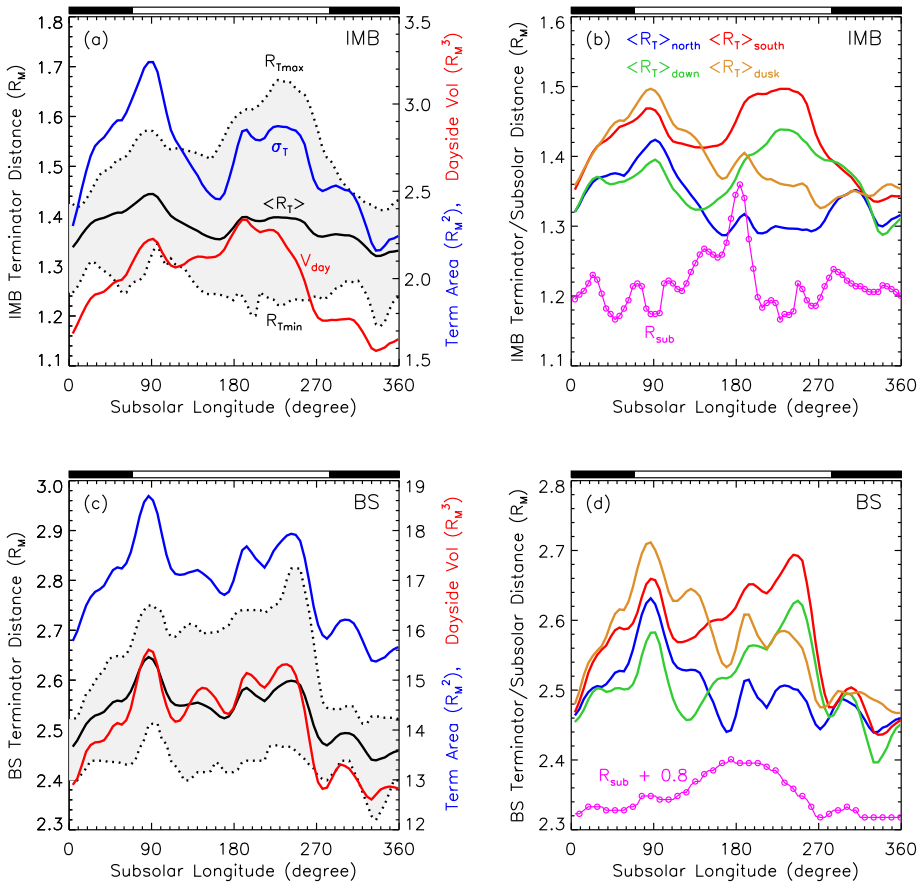

Figure 1. The MHD-model-derived (top) IMB (top) and (bottom) BS locations as a function of subsolar longitude during 16 May 2005. In the left column, the black lines show the mean boundary distances (left axis) to the Sun-Mars line at the terminator, and the gray shaded areas are bounded by the minimum and maximum terminator distances. The blue and red lines represent the terminator cross section areas (SZA=90°) and the bounded dayside volumes (SZA≤90°), respectively, above the inner MHD model boundary of 100 km altitude (right axis). In the right column, the terminator distances averaged in the MSO Northern (Z_{MSO}¿0, in blue) and Southern (Z_{MSO}¡0, in red) Hemispheres and on the dawnside (Y_{MSO}¡0, in green) and on the duskside (Y_{MSO}¿0, in brown) are shown. The magenta lines with dots show the radial distances of the boundaries at the subsolar point for comparison. Note that the BS subsolar distance has been shifted outward by 0.8 R_M in order to fit the figure scale. The white and black horizontal bars above each panel indicate time when the strongest crustal field region is on the dayside and on the nightside, respectively.

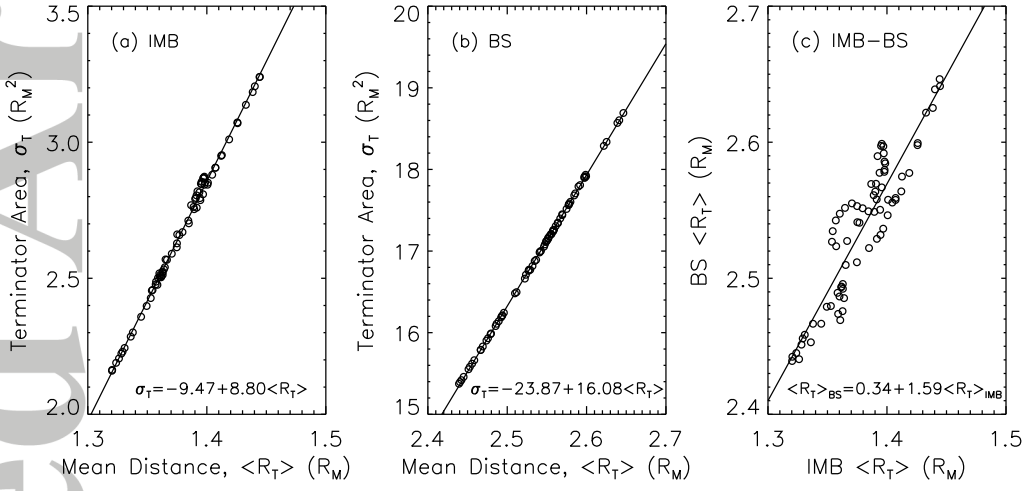

Figure 2. Scatter plots showing the correlation between the mean distance and the boundary cross section area above 100 km altitude in the terminator plane for (a) the IMB and (b) the BS. Panel (c) shows the scatter plot of the IMB terminator mean distance versus the BS mean distance. Each symbol stands for the calculation results with a cadence of 20 min over one Mars rotation period. The best fit regression lines and equations are provided.

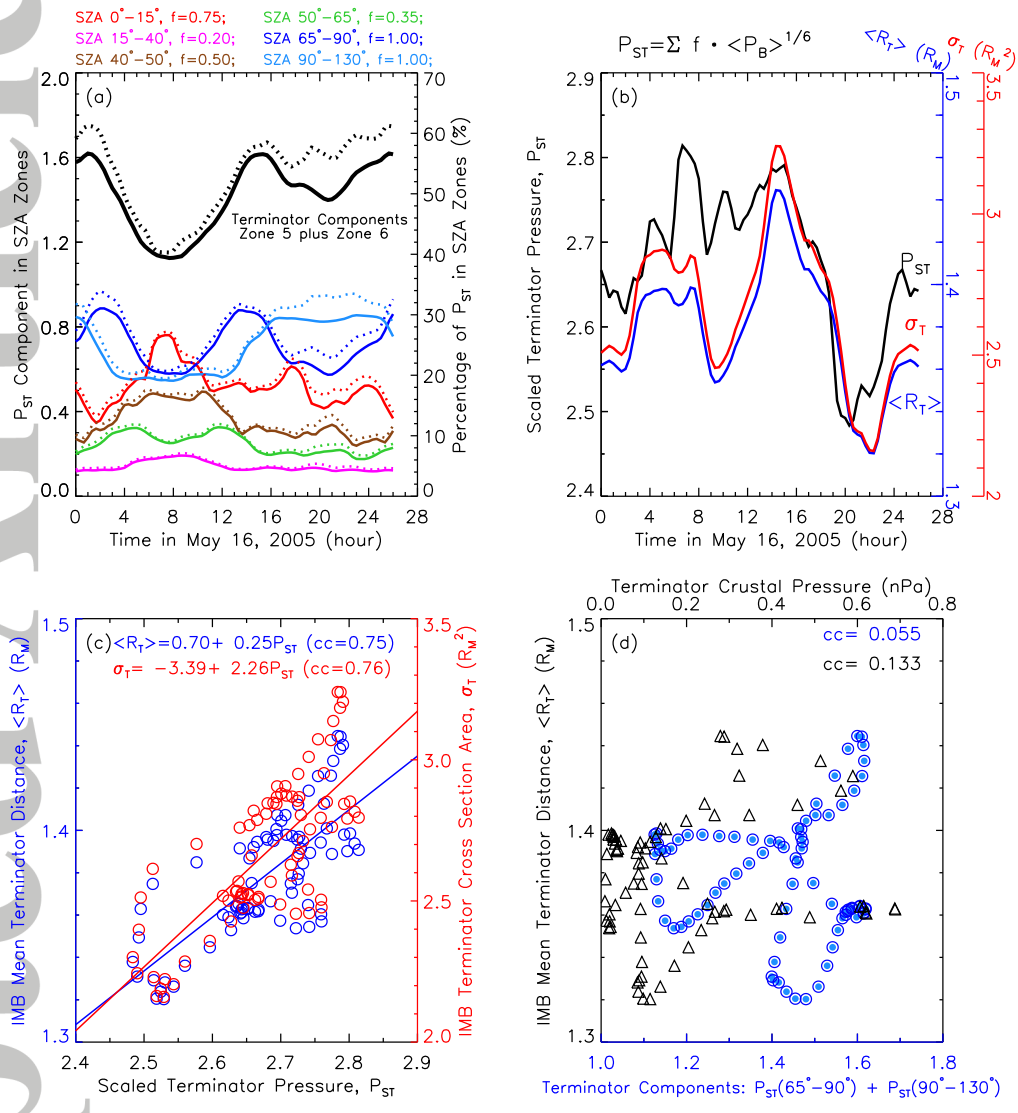

Figure 3. The scaled terminator pressure ($P_{\rm ST}$) of the crustal magnetic field as empirically defined in equantion (3), and its relationship with the IMB mean distance ($\langle R_T \rangle$) and cross section area (σ_T) at the terminator. Panel (a) shows the time variation of the $P_{\rm ST}$ components in 6 SZA zones, whose ranges and weights are marked above the panel. The black solid line represents the combined $P_{\rm ST}$ components in two adjacent SZA zones near the terminator (i.e., 65°-90° and 90°-130°). The dotted lines shows the percentage of each component in relation to the total (right axis). Panel (b) shows the time variation of $P_{\rm ST}$ in total (in black, left axis) as well as IMB $\langle R_T \rangle$ and σ_T (right axes in blue and red, respectively). Panel (c) examines the correlation between $P_{\rm ST}$ and $\langle R_T \rangle$ (left axis in blue) and between $P_{\rm ST}$ and σ_T (right axis in red), with the best fit results and correlation coefficients given. Panel (d) shows the scatter plot of IMB $\langle R_T \rangle$ versus the combined $P_{\rm ST}$ terminator components (same as the black line in panel a, see bottom scale in blue) as well as the normal crustal magnetic pressure averaged over a narrow SZA range of 85°-95° (top scale in black). The correlation coefficients are given in the panel.

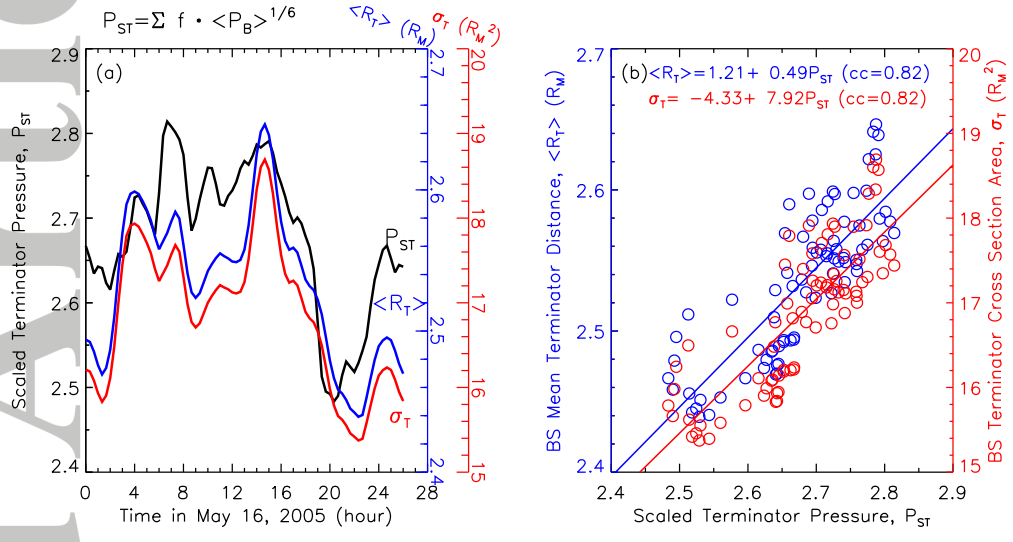

Figure 4. Similar to Figure 3b and Figure 3c but for the BS. The scaled terminator pressure is the same as in Figure 3.

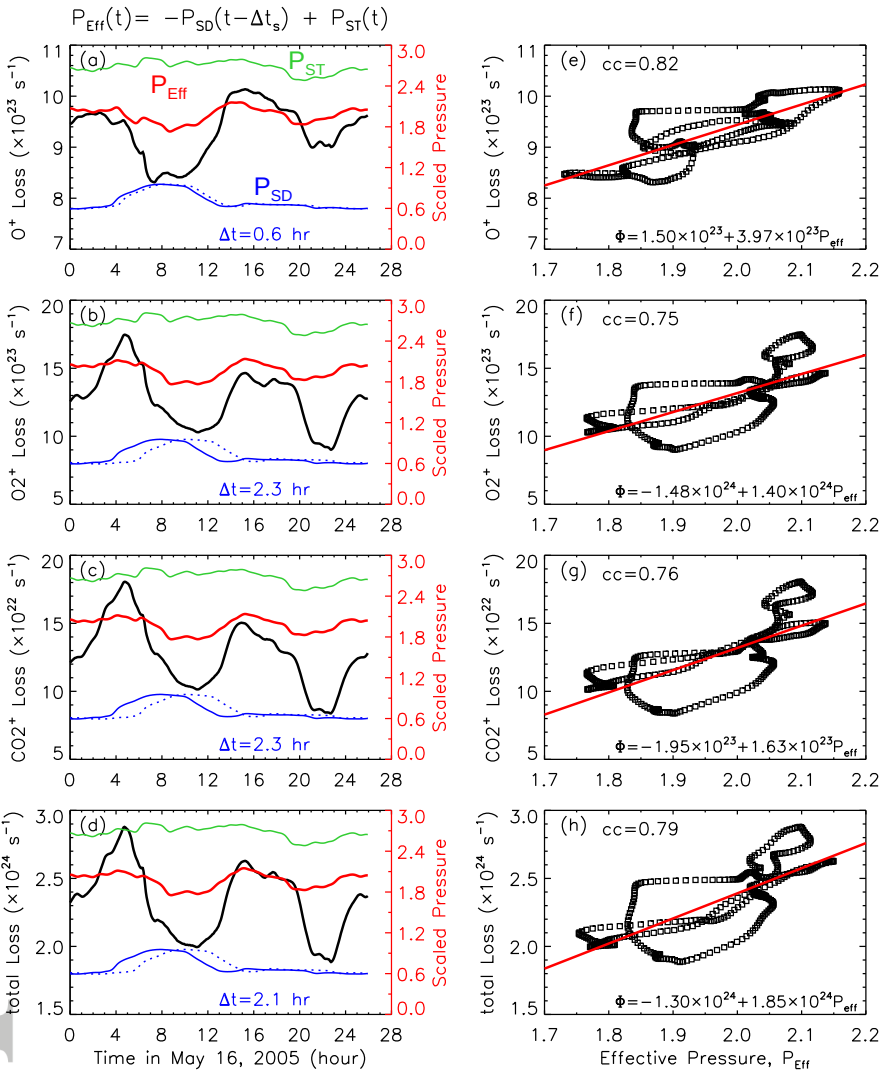

Figure 5. (from top to bottom) The correlation between the scaled effective pressure $P_{\rm Eff}$ as empirically defined in equation (5) and the MHD-calculated loss rate for O^+, O_2^+, CO_2^+, and total ions, respectively. In the left column, the black lines represent the ion loss rates integrated over a spherical surface of 6 R_M, with a scale on the left axis. The red lines represent $P_{\rm Eff}$, while the solid blue and green lines show its dayside and terminator components, $P_{\rm SD}(t)$ and $P_{\rm ST}(t)$, respectively. The blue dotted lines show the time-lagged $P_{\rm SD}(t\text{-}\Delta t_s)$. These scaled pressures are displayed using the right axis. In the right column, the correlation is examined through scatter plots. The points are sampled every 4 min. The best fit regression lines and the correlation coefficients are marked.

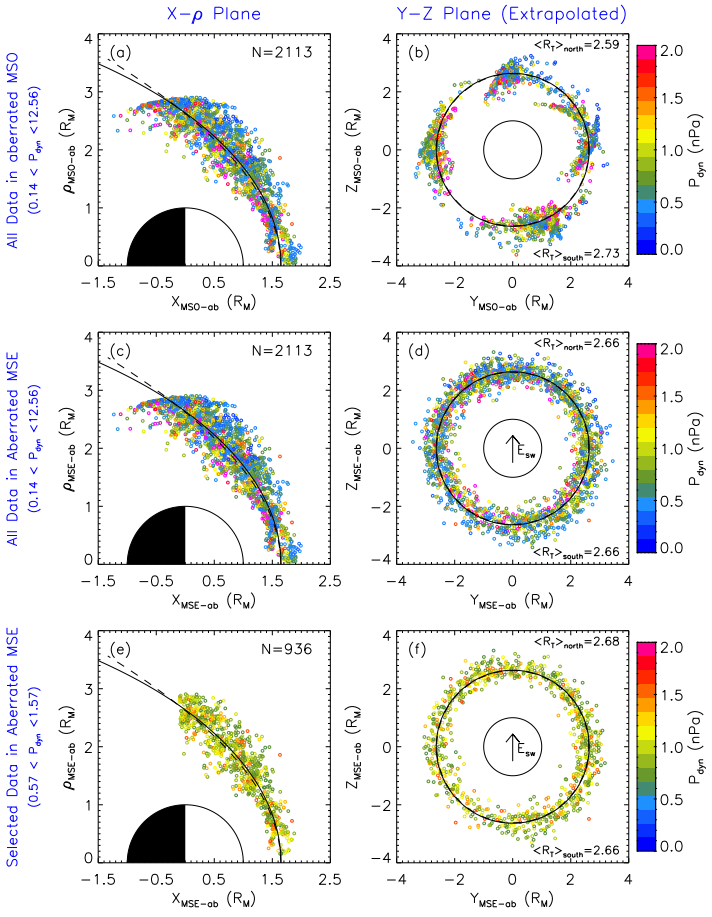

Figure 6. The BS crossing of MAVEN (left) organized in cylindrical coordinates relative to the Mars-Sun line and (right) extrapolated to the terminator plane assuming a conic section shape. The top and middle panels are shown for all the BS crossings in the aberrated MSO and MSE coordinate systems, respectively. The color of the symbols represents the orbit-averaged upstream solar wind dynamic pressure $P_{\rm dyn}$. The bottom panels are similar to the middle panels but for a subset of the BS locations when $P_{\rm dyn}$ deviates from the upstream input of the MHD model by less than 0.5 nPa. In the subset, we also exclude the boundary crossing that happens on the nightside (X≤-0.1 R_M) and over the subsolar region (SZA ≤5°). The number of data points is shown in the left column panels, while the mean terminator distances in the Northern and Southern Hemispheres are shown on the corners of the right column panels. Our conic section fit to the MAVEN dayside observations and the *Vignes et al.* [2000] model are superposed in solid and dashed lines, respectively, for reference. The parameters of our fit are X_0=0.42 R_M, L=2.303 R_M, and ϵ=0.872. The solar wind convection electric field direction is marked in panels (d) and (f).

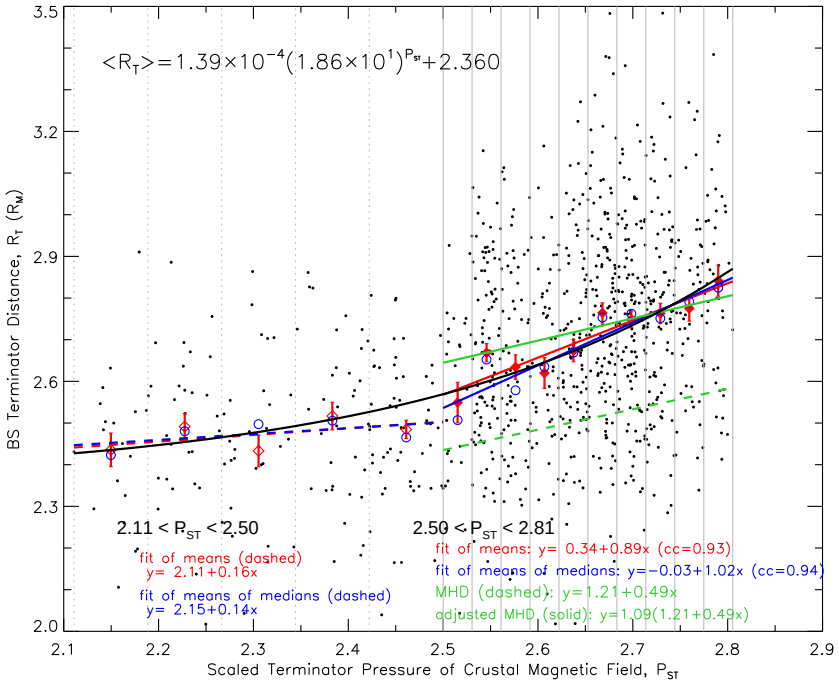

Figure 7. The MAVEN-derived BS terminator distance (R_T) in Figure 6f is reorganized as a function of the crustal field scaled terminator pressure (P_{ST}). For P_{ST} values lower/higher than 2.50, the data points are sorted into 5 coarse bins and 10 fine bins, respectively. The red diamond positions correspond to the center P_{ST} bin values and the arithmetic mean R_T values of the data points therein, with the standard errors of the mean shown as the error bars. The blue circles are similar but represent the mean values of the median distances in 45°-clock angle sectors on the Y-Z plane (see the text). The red and blue solid lines are the best fit regression lines to the red and blue symbols in the fine bins, respectively. The red and blue dashed lines are the fit to the mean positions in the coarse bins. The black curve is the least square exponential fit to all the red diamonds, with the equation shown at the top left corner. The dashed green line is the model predicted P_{ST}-$\langle R_T \rangle$ relationship (as previously shown by the blue line in Figure 4b), while the solid green line represents a 9% increase after taking into account the solar EUV difference between the model and data.

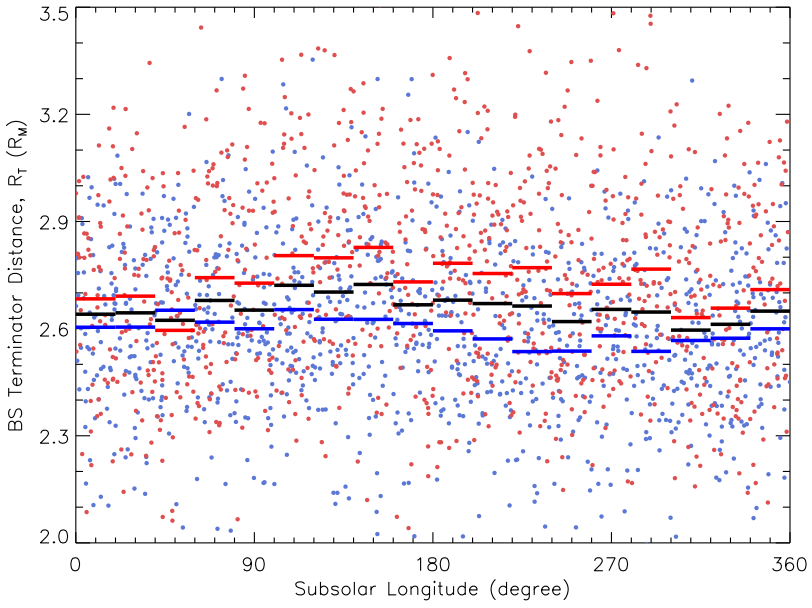

Figure 8. MAVEN-derived terminator distance of the BS versus subsolar longitude. The red and blue dots represent the observations taking place in the MSO Southern and Northern Hemispheres, respectively. The horizontal bars mark the mean values within 20° subsolar longitude bins, with the colors of red/blue/black standing for the averaging in the Southern/Northern/all Hemisphere, respectively. Note that the reverse order of the north-south asymmetry in the 40°-60° bin is statistically insignificant according to Student's t-test.